JCIS Open 23 (2026) 100188

Contents lists available at ScienceDirect

JCIS Open

journal homepage: www.journals.elsevier.com/jcis-open

Electric-field deformation of polymer droplets resolved by pressure-curvature

Mike Dohmen [a,*], Andreas Heinrich [a], Cornelius Neumann [b]

[a] Aalen School of Applied Photonics (AASAP), Aalen University, Beethovenstraße 1, Aalen, 73430, Germany
[b] Light Technology Institute (LTI), Karlsruhe Institute of Technology (KIT), Engesserstrasse 13, Karlsruhe, 76131, Germany

ARTICLE INFO

Keywords:
Electrohydrodynamics
Polymer droplets
Micro optical components
Pressure-curvature analysis
Effective surface charge
Finite element method

ABSTRACT

The electric-field deformation of polymer droplets, broadly known as electrohydrodynamics (EHD), offers significant advantages for fabricating micro-optical components, such as adaptive lenses and custom optical surfaces, due to their smooth surfaces and ability to form freeform surfaces. When utilizing UV-curable polymers, these droplets can be cured in an electrically deformed state, yielding solid freeform microlenses. A critical requirement for these technologies is the ability to accurately model the final droplet shape, as the interface curvature directly determines the optical performance of the resulting optical component. This paper introduces a novel framework for resolving the electric-field deformation of polymer droplets through pressure-curvature analysis, extending the foundational Young-Laplace equation to incorporate hydrostatic and Maxwell pressures derived from 2D Finite Element Method (FEM) simulations. A critical component of this methodology is the explicit inclusion of an optimized effective surface charge σ_s, which is crucial for achieving high prediction accuracy in leaky dielectrics. Our analysis demonstrates that accounting for these charges, originating from the Maxwell-Wagner effect, reduces the shape prediction error by up to a factor of two. Validated through experiments using the UV-curable polymer PR48 and oleic acid across various electrode configurations and applied voltages, the model achieves a low average Root Mean Square Error (RMSE) in the range of 10 – 50 µm for the final droplet contour. The effective surface charge exhibits a predictable, linear dependence on applied voltage for leaky dielectrics. This computationally efficient 2D approach offers rapid estimation for micro-optical component fabrication.

1. Introduction

When a liquid dielectric droplet is subjected to a high electrical field, the droplet deforms, which is broadly known as electrohydrodynamics (EHD). In the case of a polymer, this effect can be used to fabricate micro-optical components that offer advantages for creating adaptive lenses and custom optical surfaces due to its smooth surface, needing no postprocessing [1], [2], [3], [4], [5], [6], [7], [8]. When the droplet is made from an ultraviolet (UV) curable polymer, the droplet can be cured in an electrically deformed state yielding a solid freeform microlens. A critical requirement for these technologies is the ability to predict the final droplet shape, as the interface curvature directly determines the optical performance of the optical component.

The fundamentals of EHD have been researched thoroughly, particularly regarding the development and morphology of Taylor cones [9], [10], as well as droplet generation in E-Jet printing using phase field simulations [11]. Accurately capturing such dynamic deformations typically relies on advanced interface tracking methods, such as coupled incompressible smoothed particle hydrodynamics and finite volume methods [12]. Nonetheless most multifluid tracking models are computationally very expensive. Other techniques like Electrowetting on Dielectric (EWOD), while well established, are primarily capable of modifying the contact angle using the Lippmann-Young equation rather than predicting a full freeform contour which is induced by the Maxwell stress Tensor [13]. Recent analytical and numerical investigations have further refined this understanding by examining droplet dynamics in highly complex environments. Specifically, the influence of time-periodic and superposed AC/DC electric fields has been shown to critically modulate mean deformation, interfacial flow velocities, convective heat transfer, and electro-coalescence dynamics [14], [15], [16], [17]. Concurrently, studies on spatially confined systems have demonstrated that the proximity of boundaries significantly alters the

* Corresponding author.
E-mail address: mike.dohmen@hs-aalen.de (M. Dohmen).

https://doi.org/10.1016/j.jciso.2026.100188
Received 22 December 2025; Received in revised form 21 April 2026; Accepted 15 May 2026
Available online 28 May 2026

electric potential and surface charge density, profoundly affecting the equilibrium morphology of both simple and compound droplets [18], [19].

Consequently, there has been relatively little research on predictive models describing droplet behavior in non-uniform electric fields. The foundational leaky dielectric model of Taylor, often coupled with the Young-Laplace equation, provides an accurate description of droplet deformation under electric fields [20], [21]. However, these approaches, such as the widely-used Axisymmetric Drop Shape Analysis (ADSA-EF), are limited to axisymmetric systems [22], [23]. As a result, they are unable to capture non-axisymmetric deformations involving complex electrode geometries which would extend the shapes for optical components particularly for specialized applications. While fully coupled 3D FEM models can simulate such complexities, they are computationally expensive, and often only 2D shadowgraphy images of the droplets are available, making a 3D simulation impossible or reliant on the 3D shape reconstruction algorithm.

This paper addresses this gap by introducing a novel framework to iteratively calculate the droplet shape from an initial shape and the electrical field. Our methodology is built upon a physics-based pressure-curvature balance that extends the Young-Laplace equation to include hydrostatic pressure and the Maxwell pressure calculated from a 2D finite-element-method (FEM) simulation. One significant component of our model is the explicit inclusion of the optimized effective surface charge parameter σ_s. The inclusion of these Maxwell-Wagner surface charges at the leaky dielectric interface is a critical physical component in our shape modeling. Accounting for these charges is not a minor correction; it substantially improves the model's predictive accuracy, reducing the error by up to a factor of two. To validate this approach, the following section details the specific materials, experimental setups, and the step-by-step computational methodology employed in this study.

2. Materials and methods

A multi-stage procedure is outlined for characterizing and predicting the deformation of polymer droplets caused by electric stress. First the experimental apparatus, materials used, and the initial image processing pipeline required to extract the droplet contour (Section 2.1) are presented. Subsequently, we detail the numerical techniques for robust curvature extraction and contour reconstruction from this data (Section 2.2). The underlying physical principles governing the droplet shape, including the augmented Young-Laplace pressure balance, are then established (Section 2.3). Following this, we describe the FEM model used to calculate the electrical pressure term (Section 2.4). Finally, Section 2.5 details how these individual components are integrated into a complete, iterative framework to predict the final droplet shape and optimize key physical parameters.

2.1. Experimental setup and materials

The principal method that is used in this study is based on captured images of the deformation of droplets. The image acquisition and subsequent contour extraction method is shown briefly in Fig. 1. The experimental setup can deform liquid droplets by applying a large electric field using an anode and a cathode. It can capture images using shadowgraphy using a diffuse LED and a calibrated camera system. As shown in Fig. 1, from these shadowgraphy images the droplet contour can be extracted and interpolated, so that the coordinates of the droplet as well as the coordinates of the anode contour in real-word coordinates are known. The experimental setup is described in the previous works by Dohmen et al. [24], [25].

Images recorded with the experimental setup undergo a multi step processing pipeline to extract the geometric data required for the prediction model. First, the raw images are corrected for lens distortion using intrinsic camera parameters obtained via the Zhang calibration technique. The images are then binarized to create a high-contrast mask that segments the droplet and anode profiles from the background. From this mask, the final, coordinates for the contours are extracted using the Polar-Based Contour Approximation (PBCA) method. This approach transforms the contour into a polar coordinate system, allowing a b-spline to be fitted to the radius as a function of the polar angle. The resulting smooth curve is then transformed back into Cartesian coordinates. This entire image processing workflow provides the initial discrete coordinates (x, y) for the subsequent analysis. The sampling for the discrete points in this work is 500.

To assess the model that will later be used to predict the deformed droplet shapes, experiments were performed using two distinct electrode configurations. The first setup, shown in a close-up view in Fig. 2 (a), used a single precision pin as the anode, while the second configuration, depicted in Fig. 2 (b), utilized a dual pin anode with a separation of 2.54 mm. These configurations were specifically selected to validate the performance under both simple and more complex electric field geometries. For each configuration, a series of measurements was performed at multiple discrete anode positions. A representative experimental image for the single pin setup is shown in Fig. 2 (c), and for the dual pin setup in Fig. 2 (d). In these images, the superimposed colored markers illustrate the distinct horizontal locations of the anode in relation to the droplet, with a step d_a increment of 1.5 mm between positions. From left to right the position numbers go from 1 to 5.

Since the ultimate goal of this setup is to fabricate microlenses using UV-curable resin, we therefore select this type of polymer as the primary material. It is an acrylate based self-mixed Autodesk PR48 [26]. This modified composition is designated as PR48 or resin in this study. For the simulations the permittivity needs to be known, which was measured by Flucon GmbH (Bad Lauterburg, Germany) using the

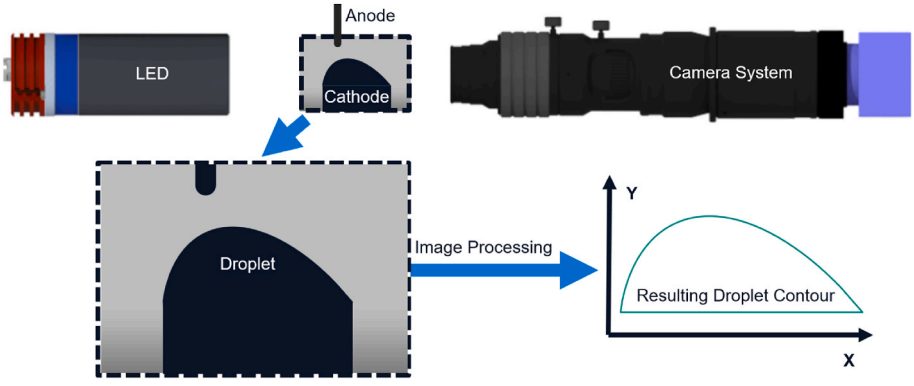

Fig. 1. The setup consists of a shadowgraphy system where a droplet, positioned between a movable anode and a fixed cathode, is illuminated by a diffuse LED. The resulting shadow is captured by a calibrated camera system. Through a series of image processing algorithms, the 2D contour of the droplet is extracted from the image and is converted into real-world coordinates, which serve as the input for the shape prediction model.

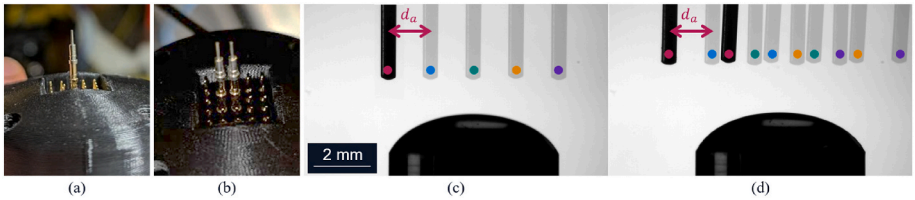

Fig. 2. (a) View of the single anode. (b) View of the dual anode. (c) Shadowgraphy image of the single anode, droplet and cathode with the experiment positions marked in color. (d) Shadowgraphy image of the dual anode, droplet and cathode with the experiment positions marked in color.

EPSILON + dielectric meter. This resulted in a value of $\epsilon_{PR48} = \epsilon_{resin} = 12.77$. The conductivity was also measured to be $\sigma_{PR48} = 1.82 \cdot 10^{-6} \frac{S}{m}$. To validate our approach with different material, experiments were also conducted with oleic acid. Unlike the leaky dielectric polymer, oleic acid serves as a control, because it is a good insulator. The permittivity of oleic acid is taken from literature as $\epsilon_{OleicAcid} = 2.46$ [27] and the conductivity is $\sigma < 2 \cdot 10^{-8} \frac{S}{m}$ [28].

2.2. Curvature extraction and contour reconstruction

While the initial contour coordinates provided by the PBCA method accurately capture the droplets overall geometry, they are not directly used for physical modeling due to inherent numerical artifacts. To derive a physically meaningful curvature profile, we therefore employ a stepwise optimization process. This process is designed to first address high-frequency numerical noise with a filter, then enforce geometric boundary conditions through a robust reconstruction algorithm that uses the shooting method and finally incorporate the governing physical laws of surface tension and gravity before applying a flexible spline correction to account for any residual deviations.

The curvature of the approximated droplet contour (x,y) can be calculated by Ref. [29]:

$$\kappa = \frac{\left|\frac{d^2y}{dx^2}\right|}{\left(1 + \left(\frac{dy}{dx}\right)^2\right)^{\frac{3}{2}}} \tag{1}$$

With κ as curvature, $\frac{dy}{dx}$ and $\frac{d^2y}{dx^2}$ are the first and second derivative of y with respect to x. Since the contour coordinates are discrete points, this process must be carried out numerically. Due to the knot nature of the spline interpolation, the curvature of the approximated droplet contour is oscillating around the real curvature, as seen in Fig. 3 as blue dashed curve. From a physical perspective, this cannot represent the true curvature, as a droplet will naturally minimize its surface area, resulting in a non-oscillating smooth curvature. To address this, the curvature is filtered using a Savitzky-Golay filter, because this class of filters is good for smoothing signals, without distorting the underlying shape [30]. The specific parameters are provided in the Supporting Information.

The objective function for this optimization consists of two terms, an accuracy term, the Root Mean Square Error (RMSE), which ensures the reconstructed contour remains true to the measured shape, and a smoothness term, which acts as a regularization penalty. This penalty is applied to the second derivative of the curvature to enforce a physically smooth interface. The detailed description of the regularization is in the supplementary material.

Fig. 3 shows an exemplary result of the grid search used for this optimization. The blue dashed line represents the initial, noisy curvature κ, while the red dash-dotted line is the final, smoothed curvature $\kappa_{smoothed}$. The faded lines depict all other combinations evaluated during the grid search. As the figure illustrates, despite the filtering, the curvature retains minor, low-frequency oscillations. These are particularly noticeable at the boundary points, an issue that will be addressed subsequently by incorporating physical constraints of the droplet.

To obtain a physically realistic droplet profile, the complete contour is reconstructed from the optimized curvature using the Frenet-Serret relations, which define a planar curve by its curvature as a function of the physical arclength. Since the numerical smoothing process introduces small geometric deviations, integrating this curvature along the arclength typically causes the reconstructed endpoint to miss the known physical boundary of the droplet on the cathode. To strictly enforce these geometric boundary conditions, we employ the shooting method as a corrective numerical technique. This algorithm iteratively optimizes the initial contact angle and superimposes linear and quadratic basis functions onto the curvature profile to eliminate any systematic bias, minimizing the Euclidean distance between the reconstructed and the physically measured endpoint. The complete mathematical derivation of this reconstruction algorithm, including the underlying ordinary differential equations and the optimization cost functions, is detailed in the supplementary material.

The fundamental principle that a planar curve is uniquely defined by its curvature provides the mathematical basis for our reconstruction method. Physically, the curvature of a liquid interface is determined by the balance of pressures acting across it. Therefore, to accurately model the droplets shape, we must analyze the contributing pressure terms.

2.3. Pressure analysis with Young-Laplace equation and E-field

A sessile droplet which is schematically shown in Fig. 4 (a) can be described without additional forces by the classical Young-Laplace

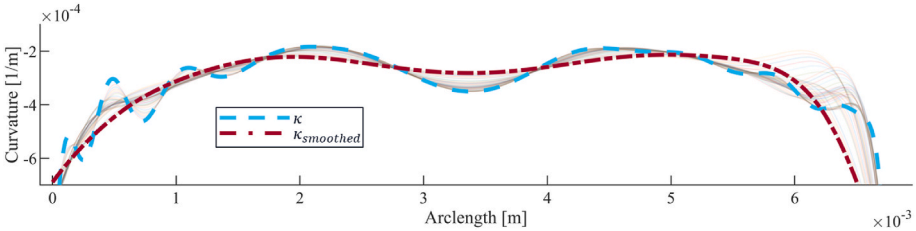

Fig. 3. Application of the Savitzky-Golay filter to smooth the experimental curvature profile. The initial curvature κ (blue dashed line), derived numerically from the spline-approximated contour, exhibits high-frequency oscillations. The faded out lines show the full range of smoothed profiles generated during the grid search over different filter parameters. The final, optimally smoothed curvature $\kappa_{smoothed}$ (red dash-dotted line) is selected based on the cost function and represents a physically realistic profile used for the subsequent reconstruction.

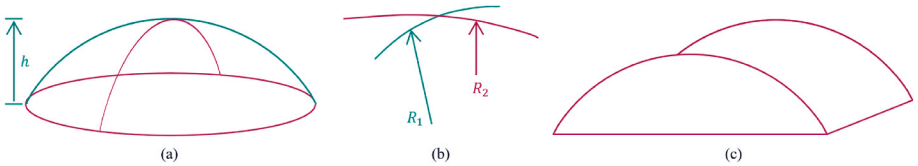

Fig. 4. (a) Schematic 3D droplet with both slices shown as well as the height. (b) Radii of a 3D droplet. (c) 2D cylinder simplification of the droplet.

equation [31]:

$$p_{inside} - p_{outside} = \Delta p = \gamma\left(\frac{1}{R_1} + \frac{1}{R_2}\right) \tag{2}$$

With p_{inside} and $p_{outside}$ as respective pressures defining the pressure outside and inside the droplet. In this paper this pressure difference is denominated as Δp. γ is the surface tension of the liquid and R_1 and R_2 are the radii of curvature of the two axes at each local droplet surface point. These two radii are shown Fig. 4 (b). The sessile droplets in this study are relatively large and operate in a high Bond number regime of $Bo \gg 1$:

$$Bo_{PR48} = \frac{\rho_{PR48} g L_c^2}{\gamma_{PR48}} = 11.9 \tag{3}$$

$$Bo_{OlAc} = \frac{\rho_{OlAc}\, g L_c^2}{\gamma_{OlAc}} = 9.6 \tag{4}$$

The density ρ was measured with a Schmidt & Haensch EDM 4000+ as $\rho_{PR48} = 1050\,\frac{kg}{m^3}$ and $\rho_{OlAc} = 893.8\,\frac{kg}{m^3}$, the characteristic length is the droplet base diameter of $L_c = 6\,mm$. The surface tension of PR48 is unknown, however, its main component, Sartomer, has a surface tension of $\gamma_{PR48} \approx 33\,\frac{mN}{m}$, which is used here as an estimate [32]. The surface tension of oleic acid is $\gamma_{OlAc} \approx 33\,\frac{mN}{m}$ [33]. These high Bond number mean, that the gravitational term must be included in the balance, to account for the deformation that is due to the deformation of the droplet by its own weight due to gravity [31]:

$$\Delta p = \gamma\left(\frac{1}{R_1} + \frac{1}{R_2}\right) + \rho g h \tag{5}$$

With g as gravity and h as the height position of the droplet surface, measured from the base to the top as seen in Fig. 4 (a). We can transform the formula into a curvature formulation by dividing all sides by the surface tension γ:

$$\frac{\Delta p}{\gamma} = \frac{1}{R_1} + \frac{1}{R_2} + \frac{\rho g h}{\gamma} = \kappa_1 + \kappa_2 + \kappa_g = \kappa_{droplet} \tag{6}$$

With κ_1 and κ_2 as respective curvature contributions of the radii, κ_g as the gravitational curvature contribution and $\kappa_{droplet}$ as resulting curvature. This curvature formulation of the pressure balance is more convenient in the subsequent sections.

As our analysis is based on a single 2D shadowgraphy image, the full 3D geometry of the droplet is not known, presenting an underdetermined problem to calculate the complete shape. The image provides the droplet's contour and thus its curvature in one plane chosen as κ_2 but contains no information about the curvature along the axis perpendicular to the viewing direction, here κ_1. To create a model from this limited data, we make the key simplification to approximate the droplet as a 2D cylindrical segment. This modeling choice is a trade-off between computational speed and physical accuracy, like how complex systems are often simplified into reduced-order models (ROM) for efficient execution [34]. This physical approximation is mathematically equivalent to setting the out-of-plane curvature contribution κ_1 to zero, which significantly simplifies the Young-Laplace curvature equation.

The degree of the validity of this simplification is dependent on the geometry of the initial droplet and the deformation. To estimate the validity of this cylindrical assumption we introduce the curvature Anisotropy ratio AR:

$$AR = \frac{\kappa_1}{\kappa_2} \tag{7}$$

A ratio of 0 would satisfy our 2D simplification. In our experimental case the ratio is close to 1, because the anode used is axisymmetric. The justification for applying this simplification to our experimental case is examined in the Discussion section.

Th 2D simplification reduces the Young-Laplace curvature equation to:

$$\kappa_{cylinder} = \kappa_2 + \kappa_g = \kappa_{sf} + \kappa_g \tag{8}$$

The curvature contribution κ_2 is from here on called κ_{sf} to reflect it as the curvature contribution of the surface tension. This characterizes the droplet form as 2D cylinder by considering both surface tension and gravity. This applies to a droplet in the absence of any external forces.

While the Young-Laplace equation describes the static shape of the droplet, the deformation process itself is dynamic. Therefore, to justify the use of a final, static equilibrium model, it is necessary to characterize the system's transient behavior. We must ensure that inertial effects, such as surface oscillations, are negligible and that the droplet settles into a stable, non-oscillating final shape. The interplay between viscous, inertial, and surface tension forces is quantified by the dimensionless Ohnesorge number (Oh):

$$Oh = \frac{\mu}{\sqrt{\rho \gamma L_h}} \tag{9}$$

A drop height of 2 mm is chosen as the characteristic length L_h, as this corresponds to the primary direction of the applied force during deformation. Using the dynamic viscosity of PR48, measured as $\mu_{PR48} = 0.6281\,Pa\,s$ with a Thermo Scientific HAAKE RheoStress 1 at 17 °C, together with the previously obtained density and surface tension values, we compute the Ohnesorge number for the PR48 resin experiments as $Oh_{PR48} = 2.39$. Because $Oh_{PR48} > 1$, the flow behavior is predominantly governed by viscous forces. This confirms that the droplet's response to the electric field is overdamped. Physically, this means the droplet deforms and reaches its final equilibrium configuration smoothly, without significant oscillations [35].

In contrast, oleic acid, with a dynamic viscosity of $\mu_{OlAc} = 37.6\,mPa\,s$ [36], has an Ohnesorge number of $Oh_{OlAc} = 0.16$. A value of $Oh_{OlAc} < 1$ indicates that inertial forces dominate and that transient oscillations may occur after the application of an electric field. To estimate the time it takes for these oscillations to decay, the viscous diffusion time τ_c is calculated, which describes the time required for momentum transport through the fluid [37]:

$$\tau_c = \frac{\rho L_h^2}{\mu} = 0.095\,s \tag{10}$$

For oleic acid, this results in a characteristic time of $\tau_c \approx 0.095\,s$. For damped exponential processes, the rule of thumb is that after a duration of $5{\cdot}\tau_c$, 99.3% of the steady state is reached [38]. This corresponds here to a time of approximately 0.5 s.

The analysis of the system dynamics justifies the use of a static modeling approach while adhering to a specific experimental boundary condition. For the polymer PR48, the assumption of a stable equilibrium is justified due to its super critically damped behavior. For oleic acid,

however, this assumption only holds if the electric field is applied for longer than 0.5 *s*.

To predict the final electrically deformed shape, our iterative method requires an accurate model of the droplets initial curvature, which is governed by the balance of surface tension and gravity. While the numerically smoothed profile from the Savitzky-Golay filter provides a good baseline, it can still contain non-physical oscillations as previously discussed. To create a more physically precise profile, we leverage the modified curvature Young-Laplace equation. The total physics-informed curvature κ_{pi} can be described by the sum of a constant surface tension component κ_{sf} and a position dependent gravitational component, κ_g:

$$\kappa_{pi} = \kappa_{sf} + \kappa_g \tag{11}$$

Theoretically, the pure surface tension contribution κ_{sf} can be calculated by subtracting the gravity contribution from the measured curvature:

$$\kappa_{sf} = \kappa_{cylinder} - \kappa_g = \kappa_{cylinder} - \frac{\rho g h}{\gamma} = constant \tag{12}$$

However, calculating this presents a challenge as it requires both the droplets density ρ and the surface tension γ. While density is known for our materials, the surface tension is unknown. This situation transforms the task into an inverse problem, where we must solve for the value of γ that best fits to the observed droplet shape. This is achieved by iteratively searching for the surface tension value that minimizes the RMSE between the experimentally measured droplet points (x^{meas}, y^{meas}) and the contour reconstructed from the physics-based model (x^{rec}, y^{rec}). The cost function $J(\gamma)$ is defined as:

$$J(\gamma) = \sqrt{\frac{1}{N}\sum_{j=1}^{N}\left[\left(x_j^{rec}(\gamma) - x_j^{meas}\right)^2 + \left(y_j^{rec}(\gamma) - y_j^{meas}\right)^2\right]} \tag{13}$$

For any value of γ used by the optimizer, the corresponding physics-informed curvature κ_{pi} is constructed. First, the gravitational contribution κ_g is calculated and subtracted from the smoothed experimental curvature $\kappa_{smoothed}$ to isolate the surface tension component κ_{sf} according to Equation (11). As illustrated in Fig. 5 (a), the resulting κ_{sf} is nearly constant across the center of the droplet but shows significant deviations at the edges due to artifacts from the initial contour fitting. To obtain a constant value we take the mean of this curve over its reliable central 60% region. This constant value for κ_{sf}, in Fig. 5 (a) called $\kappa_{sf20-80}$, is then used in Equation (12) in the place of κ_{sf} to yield the complete κ_{pi} profile. The contour is reconstructed from this profile, its RMSE against the measured shape is calculated, and the optimizer uses this error to influence its next choice for γ. Fig. 5 (b) shows how this iterative optimization of the surface tension brings the reconstructed shape progressively closer to the real droplet contour. The optimization is used with an initialization of $\gamma_0 = 30\,\frac{mN}{m}$ and terminates when change in J falls below $1{\cdot}10^{-4}$.

Having established a physics-informed model of the droplets initial curvature κ_{pi}, we must acknowledge that it remains an approximation. Minor residual deviations between this model and the measured contour remain due to physical asymmetries or simplifications inherent in the 2D surface tension model. To account for these deviations and establish a mathematically accurate geometric baseline before introducing the electrical forces, an additional, flexible correction term κ_{spline} is introduced:

$$\kappa_{cySpline} = \kappa_{pi} + \kappa_{spline} \tag{14}$$

This spline term consists of a B-spline with 10 knots. Its primary function is corrective with its coefficients optimized to minimize the final RMSE between the contour reconstructed from $\kappa_{cySpline}$ and the original measured data points (x^{meas}, y^{meas}). This step effectively corrects any minor, residual errors not captured by the physics-informed κ_{pi} model, ensuring that our representation of the initial, undeformed droplet is as accurate as possible.

Establishing this highly accurate baseline is essential for the subsequent parameter optimization. By starting with a $\kappa_{cySpline}$ that almost perfectly reproduces the initial state, we ensure that the RMSE used to find σ_s is a true measure of the electrical deformation prediction, rather than being offset by inaccuracies from an inaccurate initial shape model. Fig. 6 visually demonstrates this refinement process, comparing the initial oscillating curvature, the improved physics-informed profile κ_{pi}, and the final precisely fitted $\kappa_{cySpline}$. In this case it was a deformed droplet, because that visualizes the correction the best. This spline-corrected curvature therefore serves as the definitive starting point for the subsequent prediction steps.

When the droplet is subjected to an electric field, an additional electrical pressure deforms the interface. This effect is incorporated into our model by adding an electrical curvature term κ_e to the baseline curvature equation:

$$\kappa_{cylEl} = \kappa_{cySpline} + \kappa_e \tag{15}$$

With κ_e as electrical curvature contribution. This electrical curvature contribution can be calculated from the electrical pressure by dividing it by the surface tension γ:

$$\kappa_e = \frac{p_e}{\gamma} \tag{16}$$

This pressure p_e is induced across the interface by the electrical field and can be calculated by using the Maxwell stress tensor. The force on an area or also called traction f_e is defined as [39]:

$$f_e = T \cdot n \tag{17}$$

With n as outward normal vector and T as the Maxwell stress tensor, which is defined in its general Minkowski [40] form, which is show in further detail in the supplementary material When the material is a dielectric, the magnetic field has no contribution ($B = 0$) and the Maxwell stress tensor is defined as:

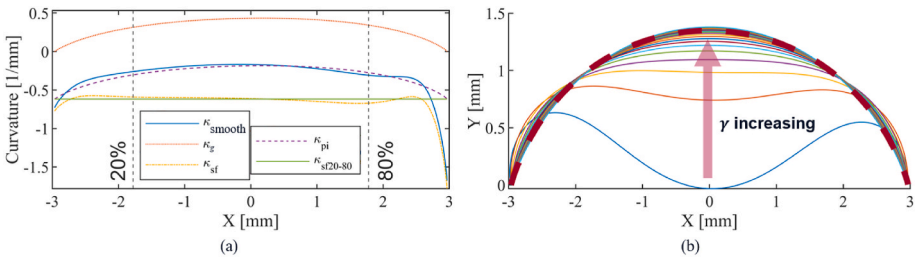

Fig. 5. Illustration of the surface tension back calculation method for a zero-field reference droplet. (a) Breakdown of the experimentally derived curvature $\kappa_{cylinder}$ into its gravitational κ_g and surface tension κ_{sf} components. The constant surface tension component $\kappa_{sf20-80}$ is determined by fitting a constant value to the central 60% of the contour. (b) Iterative reconstruction of the droplet contour by varying the surface tension γ to minimize the RMSE between the reconstructed and the original measured contour.

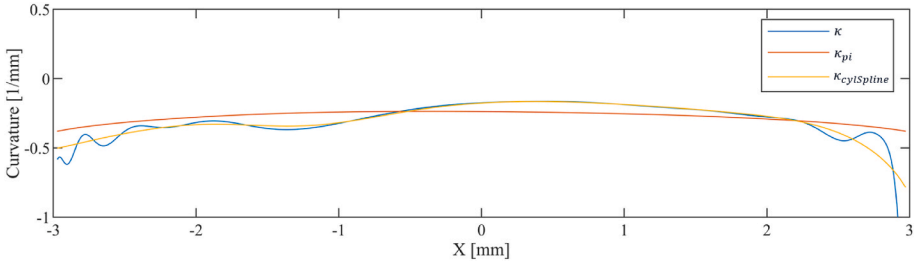

Fig. 6. Original curvature κ, the surface tension based κ_{pi} and the final with a spline curvature term corrected $\kappa_{cylSpline}$

$$T_{ij} = \epsilon\left(E_i E_j - \frac{1}{2}E^2\delta_{ij}\right) \tag{18}$$

With E as electrical field components, ϵ as absolute permittivity and d_{ij} as Kronecker delta. The only part of the traction that contributes to the pressure on a surface is the normal part of the traction [41]. Pressure is defined as a force acting solely in the direction normal to a surface, while any force acting parallel to the surface produces shear stress. Because our model describes the final, static equilibrium configuration of the droplet, there can be no persistent fluid motion along its surface. Consequently, all tangential shear forces must be balanced and therefore do not affect the droplet's shape. Thus, when evaluating the pressure balance that sets the final contour, we restrict our attention to the normal components of the electric force and disregard the tangential components in this analysis. This leads to the following equation to calculate the electrical pressure:

$$p_e = n \cdot f_e = n \cdot T \cdot n = \frac{1}{2}\epsilon\left(E_n^2 - E_t^2\right) \tag{19}$$

With E_n as normal component of the electrical field and E_t as tangential component of the electrical field at the interface. The droplet interface represents a boundary between two different, linearly polarizable dielectric media, the liquid and the surrounding air. The electrical pressure exerted on this interface is therefore the difference between the stress from the field in the air and the stress from the field in the resin. This pressure is calculated as:

$$p_e = \frac{1}{2}\epsilon_{air}\left(E_{n,air}^2 - E_{t,air}^2\right) - \frac{1}{2}\epsilon_{liquid}\left(E_{n,liquid}^2 - E_{t,liquid}^2\right) \tag{20}$$

With ϵ_{air} and ϵ_{liquid} as the absolute permittivity of air and the liquid and E_{air} and E_{liquid} the normal and tangential electrical field components in air and liquid at the interface.

In a perfectly insulating, ideal dielectric, only bound charges exist and these can be polarized, while no free charges are available to move. In contrast, real materials such as PR48 are more accurately characterized as leaky dielectrics, since they have a small but finite electrical conductivity. When a DC electric field is applied to those a small steady-state current can flow through each medium. At the interface between these two different materials, a mismatch develops between the conditions for current continuity and the electrostatic boundary conditions. This mismatch in electrical properties forces free charges to accumulate at the interface over time. This phenomenon, known as Maxwell-Wagner interfacial polarization, leads to the accumulation of a free charge layer at the interface [42].

This accumulated charge σ_s acts as an additional source, fundamentally altering the local electric field distribution at the droplet surface. While the resulting surface charge is physically expected to be non-uniform due to variations in the local electric field [40], [43], we approximate it as a single, effective value to reduce complexity.

The inclusion of this charge, combined with the complex geometry of the experimental setup, renders an analytical solution for the electric field impractical. Therefore, we employ FEM to numerically solve for the electric field distribution. The detailed setup and validation of our FEM simulation are described in the subsequent section.

2.4. Finite Element Method (FEM) electrostatics simulation

To calculate the required electrical field for the electrical pressure p_e, we used the MATLAB Partial Differential Equation Toolbox. Our FEM approach differs from some prior work, such as by Basaran et al., who used the Boundary Element Method (BEM) to solve the electric field for a physically distinct system involving a pendant drop [44]. The following paragraphs detail the configuration of our FEM model. First the geometry is set up using the coordinates of the anode and the coordinates of the droplet, which were extracted using the methodology described earlier. The width of the cathode is derived from the contact points of the droplet. Since the images are calibrated via Zhangs method, the real-world coordinates of the droplet and anode in the image are provided. This enables their accurate spatial positioning in the setup of the FEM model. Around the anode, cathode, and droplet, the space in the x-direction is multiple times the width of the image in x. This is crucial to maintain a realistic solution, avoiding distortion of the electrical field from insufficient air space around the droplet, mirroring the experimental configuration.

As discussed prior, we need to address the surface charges that stem from the Maxwell-Wagner polarization. However, since the standard formulation of the PDE Toolbox does not support the direct assignment of an idealized 2D charge layer, the effective surface charge is approximated by an equivalent volume charge density ρ_e. This is distributed within a thin shell of thickness d_{hull} that encloses the droplet interface:

$$\rho_e = \frac{\sigma_s}{d_{hull}} \tag{21}$$

With ρ_e as charge density, σ_s as surface charges and d_{hull} as hull thickness. The thickness is defined by as:

$$d_{hull} = \frac{1}{5}\overline{\Delta d_{droplet}}, \tag{22}$$

which is one fifth of the mean distance $\overline{\Delta d_{droplet}}$ between two subsequent points along the droplet contour. The factor of $\frac{1}{5}$ is chosen as compromise between calculation time and accuracy. When it is too small the mesh will get very fine, increasing computational time, while a too large hull thickness may lead to distorted results. In the supplementary material a short sensitivity analysis is shown, where the electrical pressure was calculated with the same experiment, only the hull thickness d_{hull} was changed. As the calculation time goes up significantly when the hull thickness gets smaller than $\frac{1}{5}$ the change in the electrical pressure curve is not to the same magnitude.

The model and its components are depicted as a process in Fig. 7. Fig. 7 (a) presents the model with a magnified view of the droplet contour, including the hull and its thickness. The mesh inside the hull is also displayed. Fig. 7 (b) shows a portion of the complete model's mesh, emphasizing the fine mesh size along the contour that results from the thin hull. Fig. 7 (c) illustrates the simulated electric field for an applied voltage of 3000 V between the electrodes. A further closeup of the

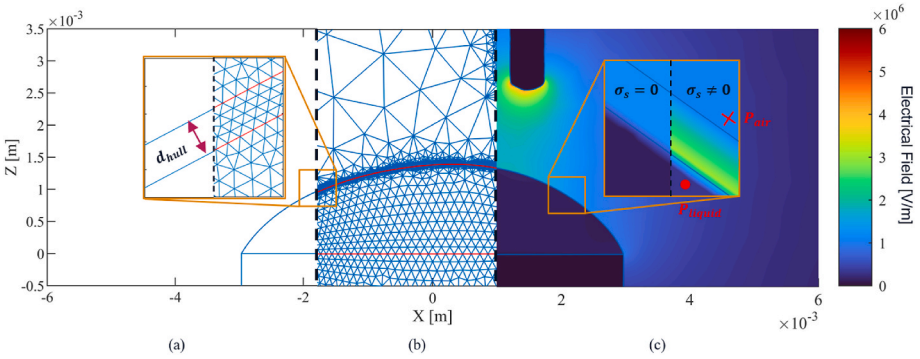

Fig. 7. (a) The geometric model used for the simulation, with a close-up view illustrating the thin hull d_{hull} constructed around the droplet interface. (b) A detailed view of the triangular mesh generated for the model. (c) A representative simulation result showing the calculated electric field distribution for an applied voltage of 3000 V. The inset provides a comparison of the electric field at the interface with no surface charge $\sigma_s = 0$ versus with an applied surface charge $\sigma_s \neq 0$, visually showing the effect on the electrical field. The points P_{air} and P_{liquid} indicate the locations just outside and inside the interface, respectively, where field values are interpolated for the pressure calculation.

contour is provided with two visualizations: one representing the electric field without effective surface charges, and the other with an example surface charge of $\sigma_s = 2{\cdot}10^{-5}\frac{C}{m^2}$. This comparison demonstrates the influence of the effective surface charge on the electric field. In addition, two points, labeled P_{air} and P_{liquid}, are indicated to mark the locations used for computing the electric field inside and outside the droplet.

To ensure a reliable numerical fem simulation, it is necessary to maintain a sufficiently high mesh quality, particularly within the thin interface hull where the effective surface charge is applied. The mesh was refined in this boundary region to accurately resolve the local electric field gradients while maintaining a stable numerical solution. Detailed mathematical definitions of the mesh quality criteria, specific element sizing parameters, and the validation of the mesh quality for our geometry are provided in the supplementary material.

The boundary conditions are applied to the meshed geometry as follows. The recorded applied voltage is assigned to the edges of the anode, and 0 V is applied to the cathode in the experiment. As mentioned above, the effective charge density is applied to the hull. To accurately model the open nature of the surrounding air and prevent artificial field confinement due to the finite computational domain, a Dirichlet boundary condition of $V = 0\ V$ was imposed on the edges of the air face. This ensures that the potential decreases appropriately to the reference value at a sufficient distance from the electrode assembly, reducing boundary induced artifacts in the calculated electric field.

This model is then solved, which results in the electrical potential and the electrical field at each node. To calculate the electrical pressure p_e from equation (20), the normal and tangential electrical field in air and resin droplet are needed. Directly at the interface, the electric field is not accurately represented, because MATLAB averages the values between the nodes, as illustrated in Fig. 7 (c) at the boundary between the droplet and the hull. The full calculation of E_t^{liquid} and E_n^{liquid} as normal and tangential electrical field inside the droplet and E_t^{air} and E_n^{air} as normal and tangential electrical field in air is outlined in the supplementary material.

To verify the consistency of the simulation and ensure the proper application of the effective surface charge σ_s, the interfacial boundary conditions for the normal displacement field and the tangential electric field were evaluated. The validation confirmed excellent agreement between the numerically calculated surface charge and the prescribed input. The detailed mathematical proof and corresponding field distributions are provided in the Supplementary Material. This validation confirms that modeling the surface charge via a volumetric charge density within a thin hull is a robust and physically consistent approach. However, it is necessary to address the significant discontinuities observed in the computed electric field at the contours edge points, an artifact evident across all validation plots. Such artifacts are a known challenge in numerical simulations, stemming from the discretization of governing equations at material interfaces or domain boundaries. In the context of this model, the effect arises because the start and end points of the droplet contour are defined in direct contact with the grounded cathode boundary. Consequently, the resulting non physical values are corrected via extrapolation from the last valid data points along the contour. This procedure is well-justified, given that these edge regions correspond to the least reliable part of the initial contour data extracted from the experimental images.

2.5. Iterative contour calculation and parameter optimization

This section details the synthesis of the preceding components into a complete, iterative framework that models and reconstructs the final, deformed contour of a droplet from an initial 2D profile and the applied electrical conditions. The core of the method involves an iterative reconstruction of the contour from its curvature, which is determined by solving a pressure-curvature balance that extends the Young-Laplace equation to include hydrostatic and electrical pressure terms. Fig. 8 presents a schematic summary of this entire workflow.

The process begins with the initial, undeformed droplet contour, which is processed as detailed in Section 2.2. This refined contour and its corresponding curvature $\kappa_{cySpline}$ serve as the input to an iterative calculation scheme. This entire process is iterated because the newly deformed contour alters the local electric field distribution, which in turn makes the recalculation of the electrical pressure necessary. For each iteration, the current contour geometry, along with the electrode configuration, material parameters, and applied voltage, are used to construct and solve a FEM analysis as described in Section 2.4. This analysis outputs the electric pressure p_e exerted on the droplet surface. The leaky dielectric Maxwell-Wagner interfacial polarization is incorporated using the effective surface charge σ_s. While the primary iterative loop can proceed without this term, achieving high predictive accuracy requires treating σ_s as a crucial parameter that is determined in a final optimization step, a process that is fully detailed at the end of this section.

A critical aspect of the iterative process is maintaining the numerical stability of the contour reconstruction. The reconstruction solves an initial value problem by integrating the curvature profile, which is sensitive to any constant offset in the curvature's magnitude. Even a minor offset, when integrated along the contour, will cause the tangent angle to drift, making the reconstructed endpoint deviate greatly from the physical boundary. This instability would prevent the algorithm from converging, even with the basic function correction.

To address this instability, we impose a numerical constraint that

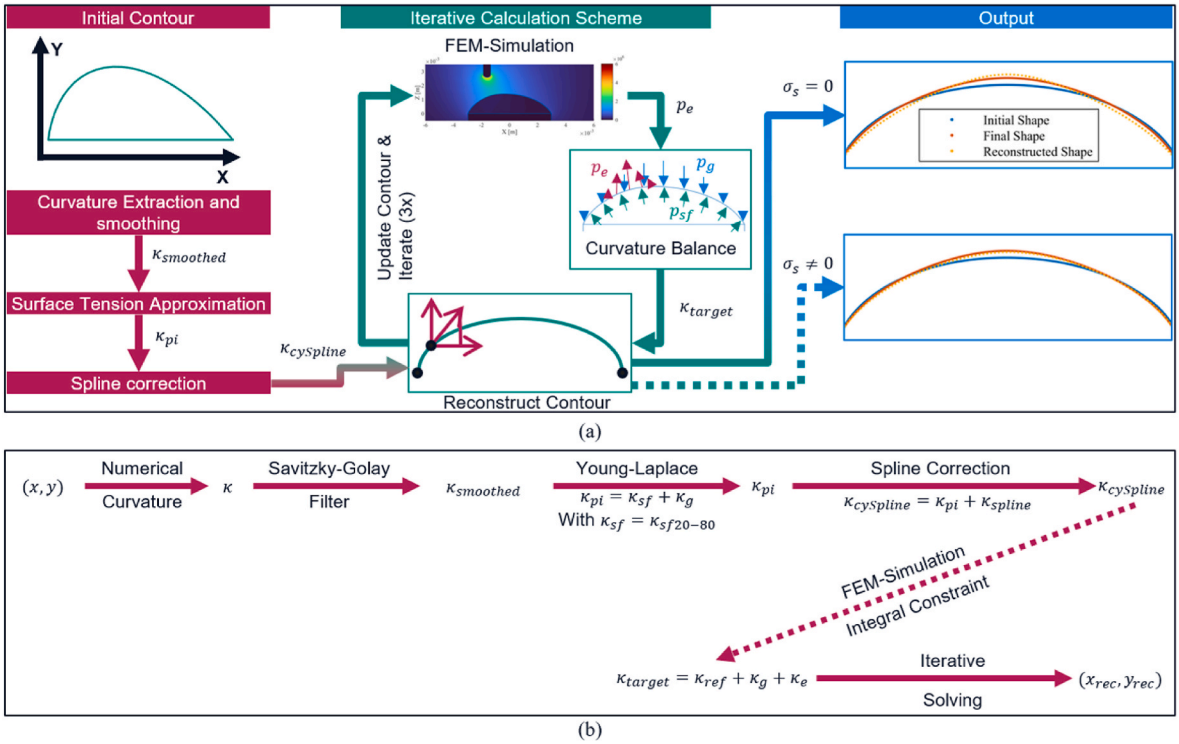

Fig. 8. (a) Flowchart of the iterative shape calculation methodology. The process begins with an Initial Contour from an image. Its curvature is extracted, smoothed to $\kappa_{smoothed}$, and refined using a physics-informed Surface Tension Approximation κ_{pi} and a Spline correction to yield a initial curvature $\kappa_{cylSpline}$. This contour enters an Iterative Calculation Scheme where a 2D FEM simulation computes the electrical pressure p_e on the current contour. This pressure is used in a Curvature Balance to define a target curvature κ_{target}, from which the contour is reconstructed. The loop is repeated three times to converge on an equilibrium shape. The final Output demonstrates the superior accuracy of the prediction in leaky dielectrics when accounting for surface charges $\sigma_s \neq 0$ compared to when they are neglected $\sigma_s = 0$. (b) A detailed, step-by-step flowchart illustrating the complete evolution of the curvature profile. The process starts with the raw experimental curvature κ and progresses through numerical smoothing $\kappa_{smoothed}$, physics-informed modeling κ_{pi}, and baseline correction $\kappa_{cySpline}$. It then shows the final, iteratively-solved target curvature κ_{target}, which explicitly includes the numerical stabilization term κ_{ref} and the electrical term κ_e.

ensures the integral of the target curvature profile with respect to the x-coordinate is conserved between iterations. It is important to note that this is a numerical stabilization technique, not a physical principle. By enforcing this constraint, we can solve for the unknown constant pressure offset κ_{ref} in the pressure balance. The target curvature κ_{target} is governed at each point by the pressure balance of the augmented curvature Young-Laplace equation:

$$\kappa_{target} = \kappa_{ref} + \kappa_g + \kappa_e \tag{23}$$

With κ_{ref} as a constant reference pressure across the interface which is unknown at the start of each iteration. The unknown constant pressure offset κ_{ref} is determined by enforcing a numerical constraint that con-

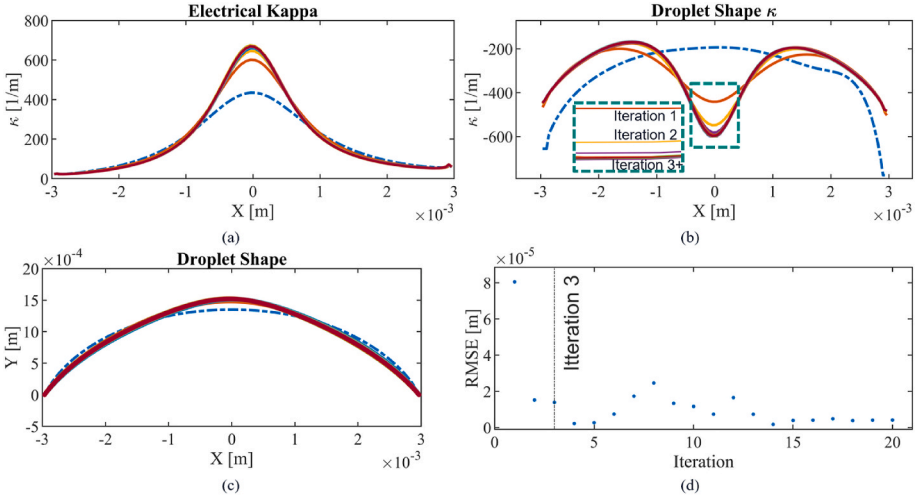

Fig. 9. Iterative convergence of the shape prediction algorithm for a representative case. (a) Electrical curvature contribution κ_e corresponding to the initial and 20 iterations for the droplet shapes. (b) Evolution of the total droplet curvature κ over 20 iterations, showing fast convergence towards a stable profile after the third iteration. (c) The corresponding change in the reconstructed droplet contour from the initial to the final predicted shape. (d) RMSE between the predicted and the final measured shape at each iteration, demonstrating that the solution stabilizes within approximately 3 iterations.

serves the integral of the curvature profile between iterations. This stabilization ensures that the reconstructed contour precisely meets the physical boundary conditions at the endpoints of the cathode. The detailed mathematical derivation of this integral constraint and the corresponding root-finding procedure for κ_{ref} are provided in the supporting material. Once the target profile is defined, the contour is reconstructed using a Runge-Kutta solver. This yields a new contour (x_{rec}, y_{rec}) that incorporates the electrical curvature.

This changed contour represents a slightly deformed droplet, which changes the electric field distribution, because the droplet is now closer to the anode. This means the algorithm needs to be run until a self-consistent equilibrium is reached. In Fig. 9 twenty iterations of the algorithm are shown. In Fig. 9 (a) the electrical curvature contribution κ_e is shown, the dash-dotted line is the curvature when the initial contour is used, and the other colors are the twenty iterations. It can also be observed that after the third iteration, the results exhibit minimal variation, indicating convergence toward an equilibrium state associated with a residual degree of uncertainty. This is shown in more detail in Fig. 9 (b) in the dashed rectangle zoom in, after the third iteration the solution is stable. The droplet shape for the iterations is shown in Fig. 9 (c). And finally, in Fig. 9 (d) the RMSE between the predicted and final contour is shown, underpinning that after the 3rd iteration the deviation does not change as much as in the first iterations.

The effective surface charge σ_s on the droplet interface is an unknown parameter that must be determined numerically. This is achieved by employing optimization algorithms to find the value of σ_s that minimizes the RMSE between our physics-based model and the observed contour of the final droplet from the experiments. The function for this optimization takes a value for the effective surface charge and executes a full simulation loop. First, the boundary conditions of an electrostatic FEM are updated with the initial charge. The model is then solved to compute the resulting electrical pressure distribution exerted on the droplet surface. From this pressure the target curvature profile κ_{target} for the droplet is calculated. Subsequently the numerical curve reconstruction algorithm generates a predicted droplet contour based on the target curvature. The RMSE between this predicted contour and the final, experimentally measured contour is then calculated and returned to the optimizer. The algorithm iteratively adjusts the surface charge value to minimize this RMSE, and the value yielding the minimum error is accepted as the effective surface charge for the system. The optimization termination tolerance is $10^{-7}\frac{C}{m^2}$ on the surface charge value and $10^{-5}m$ on the RMSE. This optimization has two goals: first to achieve an accurate reconstruction of the known final contour, and second, to determine the effective surface charge value under specific experimental conditions.

It should be noted that while σ_s is fundamentally rooted in the physics of the Maxwell-Wagner effect, it functions as an effective parameter. In this capacity, it represents the physical interfacial charge density while inherently accounting for the geometric projection and the 2D modeling simplifications necessary for computational efficiency.

3. Results

The following presents the experimental section and primary findings of our work. The section is structured into two parts. First it shows the accuracy of our surface tension measurement method as we compare it to several reference liquids and benchmarking the underlying physics-aware profile analysis. Then we showcase the capability of the full iterative model to model and predict the complete, deformed droplet shape.

3.1. Surface-tension back-calculation

To qualitatively verify the method to calculate the surface tension γ, images were taken of PR48, water, glycerol and oleic acid and then using the described methodology the surface tension was iteratively calculate. The results are shown in Table 1 as well as literature values of the surface tension for the materials [33], [45], [46].

The data indicates that while the values exhibit significant standard deviations of up to 4.72 $\frac{mN}{m}$, they qualitatively align with the expected magnitude, but they have large deviation, making the method not suitable for measuring of the surface tension. The observed deviations can most probable be attributed to the inherent assumptions in our framework, the simplification of the 3D droplet as a 2D cylindrical segment and the smoothing of the contour.

Furthermore, the final RMSE between the initial measured contour and the final reconstructed contour after all refinement steps is in the mean range of $5-10\ \mu m$. This low RMSE does not validate the physical parameter γ itself but rather confirms the high accuracy and robustness of the geometric reconstruction algorithm, ensuring that our baseline shape is a mathematically precise representation of the experimental data before the iterative prediction begins. A boxplot of the surface tension values and the RMSE measurements are shown in in the supplementary material.

3.2. Deformation experiments and model accuracy

In this section, we assess our model through experiments using two distinct electrode configurations and various materials. Our main goals are to quantify the overall modelling accuracy and to evaluate the enhancement in contour-modelling accuracy achieved by including the effective surface charge term σ_s in the model.

We conducted a series of 118 experiments using the anode configurations and the two different liquid materials PR48 and oleic acid. The selection of these materials and configurations is done to validate different aspects. The polymer PR48 is a leaky dielectric where the Maxwell-Wagner polarization is expected to play a significant role. In contrast oleic acid is a good insulator and has a small conductivity, where the Maxwell-Wagner effect should be minimal. Furthermore, these two materials have significantly different permittivities. These properties allow us to directly test our hypothesis that surface charge is a critical factor for modeling and shape prediction in leaky dielectrics. The experiments were structured into three main batches to systematically investigate the effects of voltage, voltage polarity, and electrode geometry. A total of 29 experiments were performed with a single anode on PR48 and oleic acid, respectively. These experiments were conducted at five distinct anode positions as seen in Fig. 2 (c), with three voltage stages applied as $V_{max} = \{1000\ V, 2000\ V, 3000\ V\}$. The selection of these voltage steps was motivated by prior experimental work, which established this range as optimal for observing droplet deformation behavior. The distance d_a separating two anode positions measures $1.5\ mm$. The colored points in Fig. 2 (c) denote positions 1 through 5.

For the dual anode configuration, a larger batch of 60 experiments was carried out on PR48. This configuration was chosen to test the models performance under more complex electric field. The voltage steps were expanded to include both positive and negative polarities, specifically the voltages were $V_{max} = \{-3000\ V, -2000\ V, -1000\ V, 1000\ V, 2000\ V, 3000\ V\}$. This was chosen to investigate whether the surface charge would reverse its sign. The dual anode configuration is

Table 1
Literature values and mean of measured surface tension values and standard deviation.

	PR48	Water	Glycerol	Oleic Acid
$\gamma_{literature}\left[\frac{mN}{m}\right]$	≈33	72	63,4	33
$\overline{\gamma_{meas}}\left[\frac{mN}{m}\right]$	37,82	63,15	81,46	39,4
Standard Deviation $\left[\frac{mN}{m}\right]$	0,29	4,72	1,11	0,44

shown in Fig. 2 (b) and (d).

In each experiment, the time-dependent deformation of the droplet was controlled. An identical total experiment duration of 3 s was used for all experiments. The initial state was captured before voltage application, followed by a controlled voltage ramp-up and a 1-s period at the maximum voltage V_{max} to ensure the droplet reached a stable, deformed equilibrium. The voltage was then ramped down. To rule out any influence from the transient effects of the electrical ramp-up, two different ramp durations $t_{ramp} = \{0.1\,s, 0.002\,s\}$ were tested. Our analysis showed no significant influence of the ramp durations on either the final deformation or the calculated effective surface charges, confirming that the system reached a quasi-steady-state equilibrium under these conditions. Corresponding boxplots are shown in the supplementary Material.

The initial droplet contour was obtained from the image recorded at 1 s, prior to voltage application, while the final deformed contour was taken from the image at 2 s, corresponding to the end of the constant high-voltage phase. Using this standardized procedure guarantees that all measurements are consistently derived from the undeformed and the final deformed equilibrium configurations, which serve as the essential inputs for our predictive algorithm. Using these images and the voltages from these three sets of experiments, we evaluate our predictive modeling approach. We use the algorithm two times, first without an applied effective surface charge and then with an applied effective surface charge as outlined in Fig. 8. We evaluate the shape agreement by calculating the RMSE between the real measured deformation and the predicted deformation. A surrogate optimization method is used to numerically determine the effective surface charge σ_s [47].

In Fig. 10 the result of the experiment with PR48 and both anode configurations are shown. Fig. 10 (a), (b), and (c) for PR48 and one anode and in Fig. 10(g) and (h) and (i) for the two anode configuration illustrate that the overall shape of the reconstructed contours without surface charges qualitatively approximate the actual final contour. This initial result confirms that our physical model is fundamentally valid. However, the discrepancies remain significant, particularly in the edge regions close to the contact point and at the droplets apex. The reconstructed contours with an applied effective surface charges change the shape of the contour in exactly these areas, where the deviations are the largest. These are shown in Fig. 10(d) and (e) and (f) for the one anode configuration and in Fig. 10(j) and (k) and (l) for the two anode configuration. For the experiments with oleic acid the images are similar, except a less large improvement with an applied surface charge. The contours of oleic acid and the other voltages are shown in the supplementary material.

This qualitative analysis is further deepened by the quantitative RMSE reduction when applying the effective surface charges. In Fig. 11 the surface charges and the RMSE are shown. Interestingly the calculated effective surface charge has an apparent linear dependency on the applied voltage with the polymeric PR48 as seen in the boxplots of the experiments with PR48 and one anode in Fig. 11 (a) as well as in the boxplots of the PR48 experiments with two anodes in Fig. 11 (c). For oleic acid this trend is not observed as seen in Fig. 11 (b). As evident

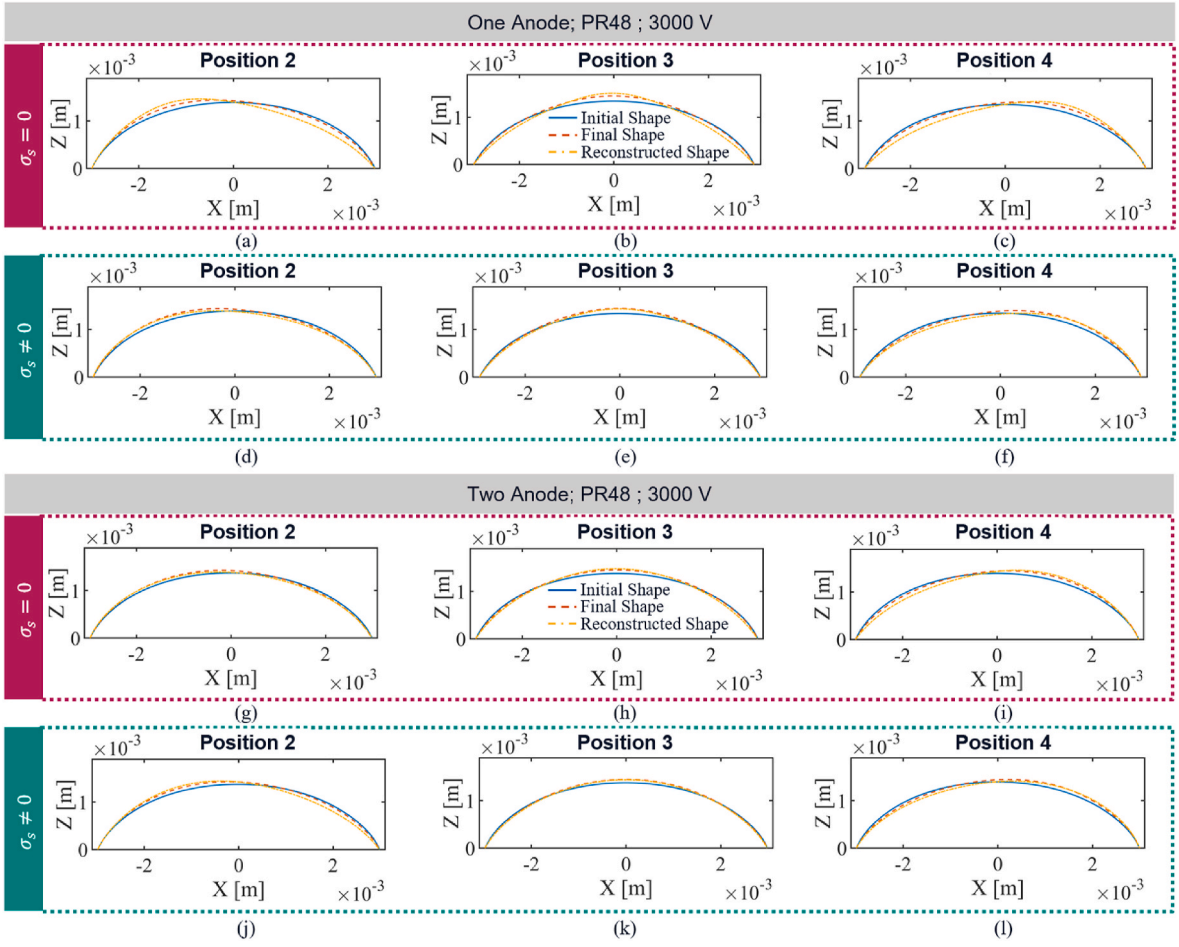

Fig. 10. Qualitative comparison of the predicted droplet shape for PR48 experiments at 3000 V under single-anode (top) and dual-anode (bottom) configurations. Each plot compares the Initial Shape (undeformed), the Final Shape (experimentally measured), and the Reconstructed Shape (model prediction). The predictions are shown without surface charges ($\sigma_s = 0$) and with an effective surface charge ($\sigma_s = 0$) determined via optimization, demonstrating a significant improvement in accuracy when the charge is included.

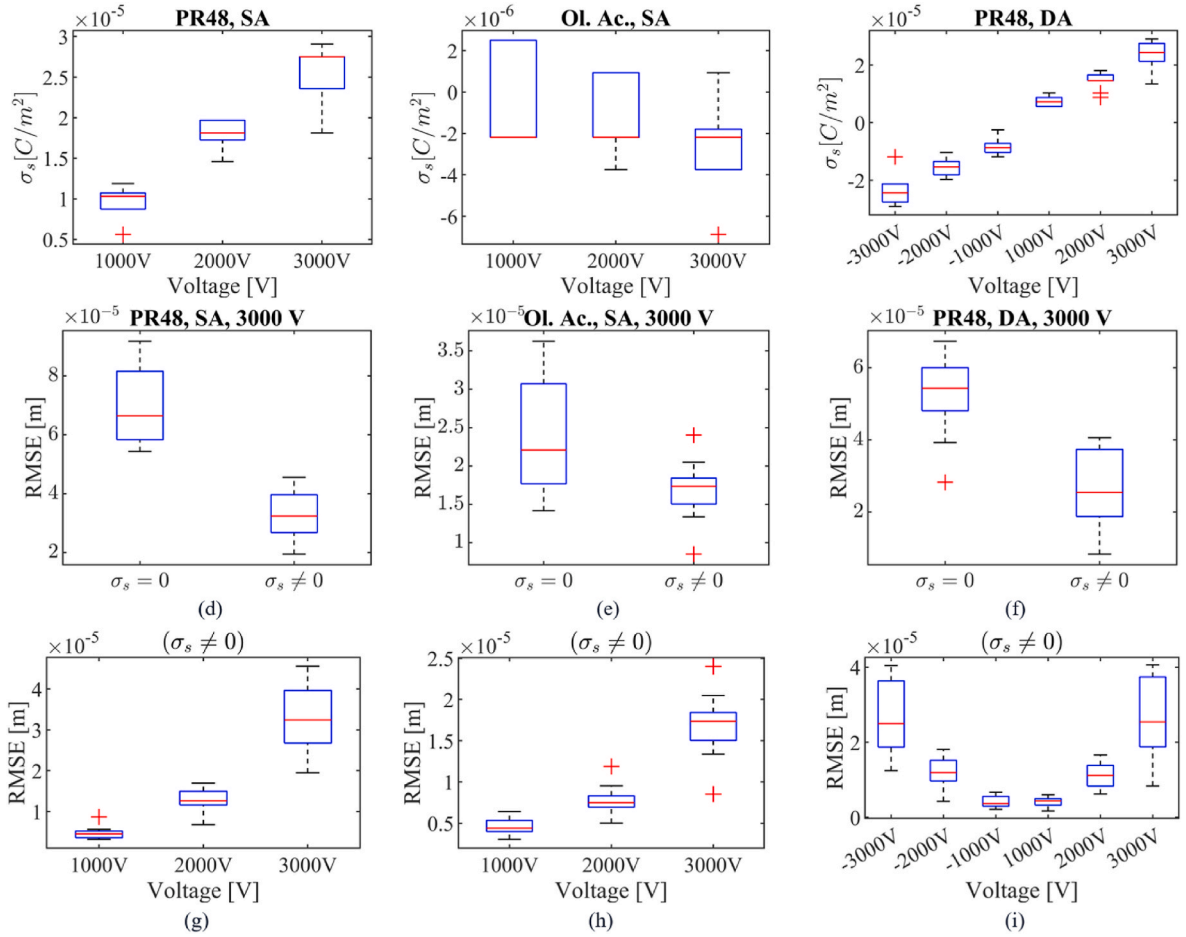

Fig. 11. Quantitative analysis of the deformation experiments and validation of the surface charge model. (a-c) Boxplots of the optimized surface charge σ_s as a function of the applied voltage. A strong linear dependence is evident for the polymer PR48 (a, c), whereas this is not observed for oleic acid (b). This supports the hypothesis of Maxwell-Wagner polarization for the "leaky dielectric" polymer. (d-f) Comparison of the Root Mean Square Error (RMSE) at 3000 V. The inclusion of the surface charge term significantly reduces the prediction error for all three experimental configurations. (g-i) RMSE of the prediction without considering surface charges across the entire voltage range. The error for the single-anode experiments correlates with the voltage, underscoring the necessity of the surface charge correction, especially at high field strengths.

from Fig. 11 (d), (e), and (f) and the RMSE, incorporating surface charges minimizes the gap between actual measurements and predicted contours. Nonetheless, some error remains between the actual final shape and the contour reconstructed using surface charges.

In Table 2 it can be seen in numbers that the RMSE values of applying and optimizing for the effective surface charge σ_s significantly enhances the predictive accuracy especially at 3000 V where the effect is the most prominent.

At this 3000 *V* peak, the mean RMSE is reduced by 53% for the PR48 single-anode configuration, by 49% for the PR48 dual-anode configuration, and by 27.6% for the slightly conductive oleic acid control. This systematic reduction confirms that accounting for interfacial charge accumulation is essential for accurately modeling the electrohydrodynamic deformation of leaky dielectrics. A comprehensive, tabulated breakdown of the position- and voltage-dependent RMSE values, alongside the localized surface charge distributions, is provided in the supplementary material. The overall final RMSE is in the range of $10 - 50\ \mu m$ with the surface charge, which is around one percent of the droplet's diameter.

Table 2
RMSE improvement at 3000 V.

	Mean RMSE ($\sigma_s = 0$) [mm]	Mean RMSE ($\sigma_s \neq 0$) [mm]
PR 48 (Single Anode)	7.02×10^{-5}	3.27×10^{-5}
PR 48 (Dual Anode)	5.22×10^{-5}	2.71×10^{-5}
Oleic Acid (Single Anode)	2.39×10^{-5}	1.67×10^{-5}

The physical validity of the proposed framework is substantiated by the correlation between the optimized effective surface charges and the applied voltage. For the PR48 experiments, the surface charge exhibits a strong positive linear correlation with the voltage, yielding Pearson coefficients of 0.93 ($p < 0.0001$) for the single-anode and 0.98 ($p < 0.0001$) for the dual-anode configurations. In contrast, the oleic acid experiments reveal a weak negative correlation with -0.36 ($p = 0.062$). These divergent trends align precisely with classical Taylor-Melcher leaky dielectric theory: the linear scaling in PR48 confirms its behavior as a leaky dielectric where charge conduction is field-dependent, whereas the negligible correlation in oleic acid is consistent with its role as a near-ideal insulator. Crucially, the fact that the optimized charge for oleic acid does not scale with the field strength suggests that σ_s functions as a physically grounded parameter rather than a mere numerical fitting constant.

However, the predictive performance is also governed by geometric constraints. As shown in Fig. 11 (g), the RMSE for the single-anode PR48 experiments correlates positively with the applied voltage, a trend notably absent in the dual-anode configuration in Fig. 11 (i). This discrepancy highlights the inherent limitations of the 2D cylindrical simplification, particularly under high field strengths. As voltage

increases, the resulting droplet deformation becomes more pronounced, causing the 3D nature of the electric field and the associated azimuthal curvatures to become the dominant sources of error. The oleic acid data further supports this hypothesis; despite the lack of correlation between surface charge and voltage, the RMSE still increases alongside deformation as seen in Fig. 11 (h). This confirms that a significant portion of the prediction error at high voltages is independent of the Maxwell-Wagner effect and must be attributed to the breakdown of the 2D approximation as the droplet transitions into a more complex 3D equilibrium shape.

Furthermore, the boxplots in Fig. 12 demonstrate that the effective surface charge is independent of the lateral anode position. As shown in Fig. 12(a)–(c), the calculated surface charge exhibits no clear positional trend across the different configurations. This geometric independence strongly supports the conclusion that the surface charge is a true physical material parameter, rather than a purely mathematical artifact compensating for 2D asymmetry.

Notably, Fig. 12 (b) highlights the specific behavior of insulating oleic acid. Its calculated surface charge is so small that it operates at the absolute resolution limit of the numerical solver, which is visually evidenced by the discrete horizontal banding in the data points. Finally, the robustness of the 2D approximation across varying asymmetric field gradients is further reinforced by the RMSE distributions in Fig. 12(d)–(f), which similarly display no distinct positional dependency.

3.3. Discussion

The primary source of error in the proposed prediction framework is from the inherent simplification of a 3D sessile droplet into a 2D cylindrical representation. To quantify the validity of this approach, we introduced the curvature anisotropy ratio in the methodology. In an ideal 2D cylindrical droplet, AR goes to zero and the model is physically exact. In contrast, our experimental setup utilizes a circular base and a round anode which ensures a quasi-axisymmetric deformation at the apex, resulting in $AR \approx 1$. Despite this significant simplification, our experimental results demonstrate that the 2D simplification is robust. This is achieved through the error correction capability of the effective surface charge, σ_s. While σ_s is rooted in the physical Maxwell-Wagner polarization, it most probable also acts as a phenomenological correction factor. It mathematically compensates for the 3D pressure deficit generated by the electric field acting in front of and behind the 2D slice. This suggests that the actual electrical pressure on the droplet is higher than the pressure estimated through our numerical approach, particularly at higher applied voltages where 3D effects become more pronounced.

This dual nature of σ_s can explain the remaining RMSE of 10 μm to 50 μm. As shown in Fig. 11 (i), the RMSE seems to have a non-linear increase with the degree of deformation. This trend indicates that when the out-of-plane components of the electrical field become more pronounced, the 2D approximation is less capable to approximate the physics correctly. However, an error of 50 μm represents only approximately 1% of the total droplet diameter, establishing $AR \approx 1$ as a proven baseline for the model.

The method offers a significant computational advantage, providing fast estimations of deformation configurations in contrast to the computational power needed to use a 3D approach. While the accuracy is expected to increase for elongated geometries with $AR < 1$, the model will likely reach its limits for droplets with a very asymmetrical base where $AR \gg 1$. Nonetheless we accept this 1% geometric discrepancy as a pragmatic trade-off.

The physical validity of the effective surface charge σ_s is substantiated by its scaling behavior across the different material systems, which aligns precisely with the underlying electrohydrodynamic stress balance. For the polymer PR48, the strong positive correlation between σ_s and the applied voltage U observed in Fig. 11 (a) and (c) is a direct manifestation of Maxwell-Wagner interfacial polarization. In such leaky dielectrics, the mismatch in conductivity and permittivity leads to a field-dependent accumulation of free charges at the interface. On the other hand, the oleic acid experiments serve as a critical physical benchmark for the limiting regime where $\sigma_s \to 0$. As a near-ideal insulator with negligible conductivity, oleic acid yields optimized σ_s values an order of magnitude smaller than those of PR48, exhibiting no significant correlation with the applied voltage as seen in Fig. 11 (b). This clear distinction shows that if σ_s were merely a numerical fitting parameter intended to compensate for the 2D geometric simplification or neglected 3D field components, it would inevitably scale with the deformation magnitude regardless of the material properties. The fact that the correlation is only present in the leaky dielectric case confirms that the

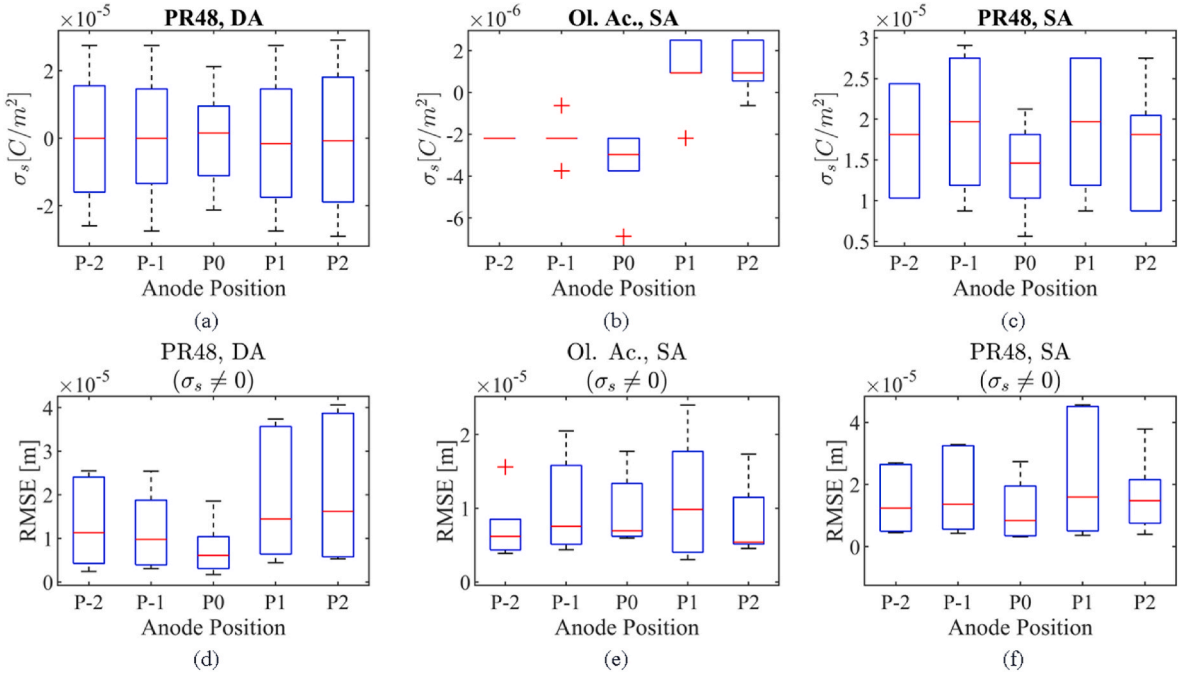

Fig. 12. Comparison of the Positional dependency of the effective surface charge and the RMSE. (a) (b) (c).

effective surface charge σ_s is a physically rooted term that allows the model to correctly distinguish between surface charge interface stresses and the purely dielectric forces acting on the interface.

A remaining refinement involves the distribution of σ_s. Although the surface charge is approximated as an effective, uniformly applied value across the entire contour, in physical reality, charges would be non-uniformly distributed due to variations in the normal electric field. This simplification likely contributes to discrepancies in regions of high field non-uniformity, although the approximation seems to be a good assumption. Furthermore, we acknowledge localized numerical artifacts, such as significant discontinuities in the computed electric field at the droplet edge points. While these non-physical values were addressed during processing, they highlight challenges at material interfaces. Future iterations may extend the electrostatic simulation to 3D to capture out-of-plane field components in highly asymmetric configurations and employ refined FEM meshing strategies to further reduce the overall prediction error.

4. Conclusion and outlook

In this work, we have presented a novel and computationally efficient framework for modeling and predicting the 2D contour of polymer droplets under strong electric fields using a single shadowgraphy image. Our methodology, which is based on a modified Young-Laplace equation that resolves the local pressure-curvature balance, incorporates hydrostatic and Maxwell pressures derived from FEM simulations. A central finding of this research is that the inclusion of an optimized effective surface charge term σ_s, reflecting Maxwell-Wagner interfacial polarization, is critical for achieving high predictive accuracy. Validation experiments using PR48 and oleic acid across various anode configurations demonstrated that the droplet contour can be reconstructed with a low average RMSE in the range of $10 - 50\ \mu m$. Crucially, incorporating the σ_s term reduced the shape prediction error by up to a factor of two, underscoring its physical significance and demonstrating a predictable behavior that can make true forward prediction for leaky dielectrics possible. While the framework also showed potential for approximating the surface tension of reference liquids, the standard deviations suggest that further refinement is required for high-precision metrology.

The accuracy of the current 2D model can be further enhanced by refining the treatment of the effective surface charge. While modeling σ_s as a constant value across the interface serves as a robust first-order approximation, a more physically rigorous approach would account for its spatial distribution along the contour. Transitioning to a spatially resolved σ_s model would better capture charge accumulation in regions of high field non-uniformity, particularly near the anode and contact points, thereby minimizing residual errors in the predicted curvature. In future research the focus is to expand this pressure-curvature framework into 3D. This transition is essential to address the 2D simplification, which remains the primary source of systematic error, especially at higher voltages where the curvature aspect ratio is very large. The benefit of such a 3D framework would be that it serves as a computationally efficient reduced-order model in contrast to fully coupled 3D electrohydrodynamic simulations, providing a fast way to determine interface equilibrium without the large computational cost.

Implementation of this 3D expansion presents two main challenges. A mathematical challenge involving the differential geometry of surface reconstruction in 3D and a validation hurdle, as the true 3D shape of a liquid interface cannot be captured by simple shadowgraphy and requires another method such as tomographic reconstruction or physically informed neural networks.

The goal of this research lies in solving the inverse problem for optical component fabrication. A validated 3D model would enable a transformative inverse design workflow. Starting from a desired target optical surface, the model would iteratively determine the necessary electrical pressure distribution, electrode configuration, and optimal voltage. This advancement would ultimately allow for the precise fabrication of true freeform optical components through electrically controlled polymer deformation.

Declaration of generative AI and AI-assisted technologies in the writing process

During the preparation of this manuscript, the authors utilized Writefull (Versions 2025.21.0 (#927) and 2025.58.0 (#1324)) and Google Gemini (Versions 2.5 Pro and 3.1 Pro) to refine the linguistic structure, improve grammar, and enhance the overall readability of the text. Additionally, MATLAB Copilot was employed to optimize the clarity and documentation of the shared MATLAB source code. Following these automated processes, the authors critically reviewed and edited the generated suggestions to ensure scientific accuracy. The authors take full responsibility for the final content and the integrity of the published work.

Funding

This research was funded by the Deutsche Forschungsgemeinschaft (DFG) grant number HE 3533/10-1.

CRediT authorship contribution statement

Mike Dohmen: Conceptualization, Data curation, Formal analysis, Investigation, Methodology, Project administration, Resources, Software, Validation, Visualization, Writing – original draft, Writing – review & editing. **Andreas Heinrich:** Conceptualization, Formal analysis, Funding acquisition, Methodology, Project administration, Resources, Supervision, Validation, Writing – review & editing. **Cornelius Neumann:** Methodology, Resources, Supervision, Validation, Writing – review & editing.

Declaration of competing interest

The authors declare that they have no known competing financial interests or personal relationships that could have appeared to influence the work reported in this paper.

Acknowledgments

The authors wish to thank the Deutsche Forschungsgemeinschaft (DFG) (grant number HE 3533/10-1) for funding and Flucon GmbH for performing the dielectric permittivity measurements.

8 Appendix

Nomenclature table

Symbol	Description	Unit
Latin Symbols		
Bo	Bond number	/
d_a	Distance between anode positions	mm

(*continued on next page*)

(*continued*)

Nomenclature table

Symbol	Description	Unit
d_{hull}	Thickness of the hull for surface charge simulation	m
E	Electric field	V/m
E_n	Normal component of the electric field	V/m
E_t	Tangential component of the electric field	V/m
e_o	Regularization error penalizing oscillations	/
e_{RMSE}	Root Mean Square Error (RMSE)	m
e_{sum}	Combined error from RMSE and regularization	/
f_e	Electric force (traction) on an area	N/m^2
g	Gravitational acceleration	m/s^2
h	Height position on the droplet surface	m
I	Number of iterations of the Savitzky-Golay filter	/
J	Cost function (RMSE) for optimization	m
L	Characteristic length (droplet base diameter)	m
n	Normal vector	/
Oh	Ohnesorge number	/
p	Polynomial order of the Savitzky-Golay filter	/
p_e	Electric pressure	Pa
Δp	Pressure difference across the interface	Pa
P_L, P_R	Left and right endpoints of the contour	/
q	Mesh quality of a triangular element	/
R_1, R_2	Principal radii of curvature of the droplet surface	m
s	Arclength along the droplet contour	m
p_1, p_2	Weighting coefficients	/
T	Maxwell stress tensor	N/m^2
V	Electric voltage	V
w	Window length of the Savitzky-Golay filter	/
t_γ	Visco capillary time	s
t_{ramp}	Ramp time for voltage application	s
V_{max}	Maximal applied voltage	V
Greek Symbols		
γ	Surface tension	N/m
δ_{ij}	Kronecker delta	/
ϵ_{PR48}	Absolute permittivity of the PR48 resin	/
$\epsilon_{OleicAcid}$	Absolute permittivity of the Oleic acid	/
ϵ_{Air}	Absolute permittivity of the air	/
θ_{left}	Left contact angle of the droplet	rad
κ	Curvature	1/m
κ_e	Electrical curvature contribution	1/m
κ_g	Gravitational curvature contribution	1/m
κ_{sf}	Curvature contribution of surface tension	1/m
$\kappa_{cylinder}$	Curvature of the 2D cylinder	1/m
$\kappa_{cylSpline}$	Spline corrected curvature	1/m
$\kappa_{smoothed}$	Savitzky-Golay filtered curvature	1/m
κ_{pi}	Physics-informed curvature	1/m
κ_{target}	Target curvature for reconstruction	1/m
λ	Regularization parameter	/
μ	Dynamic viscosity	Pa·s
ρ	Density	kg/m^3
ρ_e	Volume charge density	C/m^3
σ_s	Surface charge	C/m^2
ϕ	Angle of the tangent vector to the x-axis	rad

Appendix A. Supplementary data

Supplementary data to this article can be found online at https://doi.org/10.1016/j.jciso.2026.100188.

Data availability

I have uploaded my data/code on Zenodo:https://doi.org/10.5281/zenodo.19628855.

References

[1] K. Mishra, et al., Optofluidic lens with tunable focal length and asphericity, Sci. Rep. 4 (1) (Sep. 2014) 6378, https://doi.org/10.1038/srep06378.

[2] A.M.J. Edwards, C.V. Brown, M.I. Newton, G. McHale, Dielectrowetting: the past, present and future, Curr. Opin. Colloid Interface Sci. 36 (Jul. 2018) 28–36, https://doi.org/10.1016/j.cocis.2017.11.005.

[3] M. Kato, et al., Optically pumped and electrically switchable microlaser array based on elliptic deformation and Q-Attenuation of organic droplet oscillators, Adv. Mater. 37 (5) (2025) 2413793, https://doi.org/10.1002/adma.202413793.

[4] N.C. Lima, K. Mishra, F. Mugele, Aberration control in adaptive optics: a numerical study of arbitrarily deformable liquid lenses, Opt. Express 25 (6) (Mar. 2017) 6700–6711, https://doi.org/10.1364/OE.25.006700.

[5] S. Xu, H. Ren, Y. Liu, S.-T. Wu, Dielectric liquid microlens with switchable negative and positive optical power, IEEEASME J. Microelectromechanical Syst. - J

MICROELECTROMECHANICAL SYST 20 (Feb. 2011) 297–301, https://doi.org/10.1109/JMEMS.2010.2100032.
[6] P. Liu, X. Zhang, Q. Wang, M. Zhao, Y. Song, D. Li, Fabricating a PDMS optical lens with the interaction of a negatively-charged air-resin interface and an electric field, Colloids Surf. A Physicochem. Eng. Asp. 660 (Mar. 2023) 130876, https://doi.org/10.1016/j.colsurfa.2022.130876.
[7] C.-C. Wu, Y.-D. Tseng, S.-M. Kuo, C.-H. Lin, Fabrication of asperical lensed optical fibers with an electro-static pulling of SU-8 photoresist, Opt. Express 19 (23) (Nov. 2011) 22993–22998, https://doi.org/10.1364/OE.19.022993.
[8] S. Kuiper, B.H.W. Hendriks, Variable-focus liquid lens for miniature cameras, Appl. Phys. Lett. 85 (7) (Aug. 2004) 1128–1130, https://doi.org/10.1063/1.1779954.
[9] Y. Chen, et al., Morphology of Taylor cone in stable regime: experimental and Numerical insights, Langmuir 41 (36) (Sep. 2025) 24841–24856, https://doi.org/10.1021/acs.langmuir.5c03395.
[10] A.L. Yarin, S. Koombhongse, D.H. Reneker, Taylor cone and jetting from liquid droplets in electrospinning of nanofibers, J. Appl. Phys. 90 (9) (Nov. 2001) 4836–4846, https://doi.org/10.1063/1.1408260.
[11] D. Wang, et al., Phase field simulation of electrohydrodynamic jet droplets and printing microstructures on insulating substrates, Microelectron. Eng. 261 (May 2022) 111817, https://doi.org/10.1016/j.mee.2022.111817.
[12] Y. Xu, G. Yang, Y. Xing, D. Hu, Interface tracking simulation of multifluid flow by ISPH-FVM coupling method, Exp. Comput. Multiph. Flow 7 (4) (Dec. 2025) 465–489, https://doi.org/10.1007/s42757-024-0201-6.
[13] F. Mugele, J.-C. Baret, Electrowetting: from basics to applications, J. Phys. Condens. Matter 17 (28) (Jul. 2005) R705–R774, https://doi.org/10.1088/0953-8984/17/28/R01.
[14] B. Mohanty, A. Bandopadhyay, Numerical investigation of convective heat transfer of a droplet in a continuous medium under a time periodic electric field, Phys. Fluids 37 (8) (Aug. 2025) 082008, https://doi.org/10.1063/5.0283253.
[15] B. Mohanty, A. Bandopadhyay, Electrohydrodynamic deformation of a compound droplet in an alternating current and direct current superposed electric field, Phys. Fluids 36 (5) (May 2024) 052010, https://doi.org/10.1063/5.0209008.
[16] B. Mohanty, A. Bandopadhyay, An analytical investigation of liquid droplet deformation in a superposed electric field consisting of an alternating and a constant electric field, Phys. Fluids 36 (11) (Nov. 2024) 112034, https://doi.org/10.1063/5.0235211.
[17] B. Mohanty, A. Nayak, A. Bandopadhyay, Electro-coalescence of droplets in time-periodic electric fields: a numerical investigation, Phys. Fluids 37 (12) (Dec. 2025) 123612, https://doi.org/10.1063/5.0305991.
[18] B. Mohanty, A. Bandopadhyay, An analytical investigation of a confined compound droplet deformation in a uniform electric field using spherical harmonics, Int. J. Multiphas. Flow 191 (Oct. 2025) 105308, https://doi.org/10.1016/j.ijmultiphaseflow.2025.105308.
[19] B. Mohanty, A. Bandopadhyay, Electrohydrodynamic deformation of a confined droplet in an alternating current electric field: an analytical study, Phys. Fluids 37 (3) (Mar. 2025) 033620, https://doi.org/10.1063/5.0261782.
[20] G.I. Taylor, A.D. McEwan, L.N.J. de Jong, Studies in electrohydrodynamics. I. The circulation produced in a drop by an electric field, Proc. R. Soc. Lond. Ser. Math. Phys. Sci. 291 (1425) (Jan. 1997) 159–166, https://doi.org/10.1098/rspa.1966.0086.
[21] D.A. Saville, ELECTROHYDRODYNAMICS: the Taylor-Melcher leaky Dielectric Model, Annu. Rev. Fluid Mech. 29 (1) (Jan. 1997) 27–64, https://doi.org/10.1146/annurev.fluid.29.1.27.
[22] A. Bateni, A. Ababneh, J.A.W. Elliott, A.W. Neumann, A. Amirfazli, Effect of gravity and electric field on shape and surface tension of drops, Adv. Space Res. 36 (1) (Jan. 2005) 64–69, https://doi.org/10.1016/j.asr.2005.02.084.
[23] A. Bateni, S. Laughton, H. Tavana, S.S. Susnar, A. Amirfazli, A.W. Neumann, Effect of electric fields on contact angle and surface tension of drops, J. Colloid Interface Sci. 283 (1) (Mar. 2005) 215–222, https://doi.org/10.1016/j.jcis.2004.08.134.
[24] Modeling and simulation of custom microlenses from electrically deformed droplets [Online]. Available: https://proceedings.spiedigitallibrary.org/conference-proceedings-of-spie/13381/1338103/Modeling-and-simulation-of-custom-microlenses-from-electrically-deformed-droplets/10.1117/12.3042017.short. (Accessed 4 July 2025).
[25] M. Dohmen, A. Heinrich, C. Neumann, Polar Fitting and Hermite Interpolation for Freeform Droplet Geometry Measurement, Jul. 15, 2025 2025071179, https://doi.org/10.20944/preprints202507.1179.v1. Preprints.
[26] Autodesk_Standard_Clear_PR48_Formulation.pdf [Online]. Available: https://cdn2.hubspot.net/hubfs/1545937/Autodesk_Standard_Clear_PR48_Formulation.pdf. (Accessed 17 June 2025).
[27] R.T. Kay, W.E. Beadle, Dielectric constants of pure liquids, National Bureau of Standards, U.S. Department of Commerce, Washington, D.C., NBS Circular 514, https://nvlpubs.nist.gov/nistpubs/Legacy/circ/nbscircular514.pdf, 1951. (Accessed 17 July 2025).
[28] Emerson Automation Solutions, Manual: conductance data for commonly used chemicals, Emerson Automation Solutions, Technisches Handbuch D351911X012 (2021) [Online]. Available: https://www.emerson.com/documents/automation/manual-conductance-data-for-commonly-used-chemicals-en-68896.pdf. (Accessed 1 August 2025).
[29] E.W. Weisstein, CRC Concise Encyclopedia of Mathematics, Chapman & Hall CRC, Boca Raton London New York, 1999 [etc.].
[30] Abraham Savitzky, M.J.E. Golay, Smoothing and differentiation of data by simplified least squares procedures, Anal. Chem. 36 (8) (Jul. 1964) 1627–1639, https://doi.org/10.1021/ac60214a047.
[31] L.D. Landau, E.M. Lifshitz, L.D. Landau, Fluid mechanics. Course of Theoretical Physics, second ed., 2nd English ed., Pergamon Press, Oxford, England ; New York, 1987, 6.
[32] Arkema, "SR531 Cyclic Trimethylol-Propane Formal Acrylate: Technical Data Sheet," Arkema, 2024 [Online]. Available: https://americas.sartomer.arkema.com/assets/arkema/TDS_SR531_MDM-11104-00-AM_en_WW.pdf.
[33] L.D.A. Chumpitaz, L.F. Coutinho, A.J.A. Meirelles, Surface tension of fatty acids and triglycerides, J. Am. Oil Chem. Soc. 76 (3) (1999) 379–382, https://doi.org/10.1007/s11746-999-0245-6.
[34] Z. Dar, J. Baiges, R. Codina, Reduced order modeling, in: T. Rabczuk, K.-J. Bathe (Eds.), Machine Learning in Modeling and Simulation: Methods and Applications, Springer International Publishing, Cham, 2023, pp. 297–339, https://doi.org/10.1007/978-3-031-36644-4_8.
[35] M.A. Fardin, M. Hautefeuille, V. Sharma, Spreading, pinching, and coalescence: the Ohnesorge units, Soft Matter 18 (17) (2022) 3291–3303, https://doi.org/10.1039/D2SM00069E.
[36] D. Sagdeev, et al., Densities and viscosities of oleic acid at atmospheric pressure, J. Am. Oil Chem. Soc. 96 (6) (Jun. 2019) 647–662, https://doi.org/10.1002/aocs.12217.
[37] J.R. Melcher, Continuum Electromechanics, MIT Press, Cambridge, Mass, 1981.
[38] S. Zacher, M. Reuter, *Regelungstechnik Für Ingenieure: Analyse, Simulation Und Entwurf Von Regelkreisen*, 17. Auflage, Springer Vieweg, Wiesbaden, 2024, https://doi.org/10.1007/978-3-658-45897-3.
[39] L. Dorfmann, R.W. Ogden, Nonlinear Theory of Electroelastic and Magnetoelastic Interactions, Springer, New York, 2014.
[40] D.J. Griffiths, *Introduction to electrodynamics*, 4, in: Always Learning, Pearson, Boston, 2013.
[41] M.T. Harris, O.A. Basaran, Equilibrium shapes and stability of nonconducting pendant drops surrounded by a conducting fluid in an electric field, J. Colloid Interface Sci. 170 (2) (Mar. 1995) 308–319, https://doi.org/10.1006/jcis.1995.1107.
[42] C. Li, G. Chen, X. Qiu, Q. Lou, X. Gao, A direct proof for Maxwell–Wagner effect of heterogeneous interface, AIP Adv. 11 (6) (Jun. 2021) 065227, https://doi.org/10.1063/5.0040947.
[43] T.B. Jones, *Electromechanics of Particles*, Online-Ausg, Cambridge University Press, Cambridge, 1995, https://doi.org/10.1017/CBO9780511574498.
[44] M.T. Harris, O.A. Basaran, Equilibrium shapes and stability of nonconducting pendant drops surrounded by a conducting fluid in an electric field, J. Colloid Interface Sci. 170 (2) (Mar. 1995) 308–319, https://doi.org/10.1006/jcis.1995.1107.
[45] N.B. Vargaftik, B.N. Volkov, L.D. Voljak, International tables of the surface tension of water, J. Phys. Chem. Ref. Data 12 (3) (Jul. 1983) 817–820, https://doi.org/10.1063/1.555688.
[46] K. Takamura, H. Fischer, N.R. Morrow, Physical properties of aqueous glycerol solutions, J. Pet. Sci. Eng. 98 (99) (Nov. 2012) 50–60, https://doi.org/10.1016/j.petrol.2012.09.003.
[47] MathWorks, Surrogateopt | Global Optimization Toolbox, Oct. 2025 [Online]. Available: https://de.mathworks.com/help/gads/surrogateopt.html. (Accessed 17 October 2025).